# CCE1: Decrease in the frequency of oceanic fronts and surface chlorophyll concentration in the California Current System during the 2014–2016 northeast Pacific warm anomalies

Mati Kahru[a,*], Michael G. Jacox[b], Mark D. Ohman[a]

[a] *Scripps Institution of Oceanography, University of California, San Diego, La Jolla, CA 92093, USA*
[b] *Environmental Research Division, Southwest Fisheries Science Center, NOAA, Monterey, CA, USA and Physical Sciences Division, Earth System Research Laboratory, NOAA, Boulder, CO, USA*

A R T I C L E   I N F O

A B S T R A C T

Oceanic fronts are sites of increased vertical exchange that are often associated with increased primary productivity, downward flux of organic carbon, and aggregation of plankton and higher trophic levels. Given the influence of fronts on the functioning of marine ecosystems, an improved understanding of the spatial and temporal variability of frontal activity is desirable. Here, we document changes in the frequency of sea-surface fronts and the surface concentration of chlorophyll-a (Chla) in the California Current System that occurred during the Northeast Pacific anomalous warming of 2014–2015 and El Niño of 2015–2016, and place those anomalies in the context of two decades of variability. Frontal frequency was detected with the automated histogram method using datasets of sea-surface temperature (SST) and Chla from multiple satellite sensors. During the anomalous 2014–2016 period, a drop in the frequency of fronts coincided with the largest negative Chla anomalies and positive SST anomalies in the whole period of satellite observations (1997–2017 for Chla and 1982–2017 for SST). These recent reductions in frontal frequency ran counter to a previously reported increasing trend, though it remains to be seen if they represent brief interruptions in that trend or a reversal that will persist going forward.

## 1. Introduction

Oceanic fronts, defined as areas of sharp gradients between adjacent water masses (see Belkin, 2009 for a review), are often sites of increased physical and biological activity affecting oceanic ecosystems. In the California Current System (CCS) fronts are often created by wind-driven upwelling and the subsequent advection of the upwelled waters in the form of cold, chlorophyll-rich filaments and associated eddies (Bernstein et al., 1977; Flament et al., 1985; Strub et al., 1991; Castelao et al., 2006; Kahru et al., 2012a; Powell and Ohman, 2015a). Both the composition of planktonic communities and associated biogeochemical fluxes in the CCS are strongly affected by the presence of mesoscale fronts (Landry et al., 2012; Powell and Ohman, 2015b; Stukel et al., 2017), which also provide important habitat for mobile marine vertebrates (Scales et al., 2014) and have been proposed as proxies for pelagic diversity in the designation of marine protected areas (Miller and Christodoulou, 2014). It has been suggested that fronts increase total ecosystem biomass and enhance fishery production by channeling nutrients through alternate trophic pathways (Woodson and Litvin, 2015).

It is therefore important to understand the long-term dynamics, spatial patterns and the statistical properties of fronts and how they may be affected by interannual and long-term changes.

Here we evaluate time series of frontal frequency in light of recent years characterized by some of the largest oceanographic anomalies on record in the northeast Pacific, particularly the widespread northeast Pacific warming (the so-called "Blob") in 2014–2015 (Bond et al., 2015) and the 2015–2016 El Niño (Jacox et al., 2016). The onset of broad-scale warming in the CCS in 2014 has been attributed to anomalous winds, surface heat fluxes and likely advection of warm anomalies from the Gulf of Alaska to the North American west coast (Bond et al., 2015; Di Lorenzo and Mantua, 2016; Jacox et al., 2017). Off the southern California coast, warm anomalies were linked to local anomalous atmospheric forcing including weak winds and high downward heat flux, which appeared unrelated to the equatorial Pacific, but could be linked via atmospheric teleconnections to remote areas of the North Pacific (Zaba and Rudnick, 2016). As broad-scale warm anomalies lingered into 2015–16, they were augmented by remote ocean forcing associated with a strong equatorial El Niño event (Jacox et al., 2016;

Frischknecht et al., 2017). Due to the confluence of anomalous climatic forcing in the 2014–2016 period, the CCS experienced historic highs for sea-surface temperature (SST) anomalies (e.g., Gentemann et al., 2017), dramatic changes to phytoplankton and zooplankton abundances and community composition (Gómez-Ocampo et al., 2017; McCabe et al., 2016; Peterson et al., 2017), widespread impacts on higher trophic levels including range shifts and mortality events (Cavole et al., 2016), and restrictions or closures for several west coast fisheries (McClatchie et al., 2016; Jacox et al., 2017).

Here we investigate changes in satellite-detected SST and chlorophyll-a concentration (Chla) and in the frequencies of Chla and SST fronts in the CCS. Fronts are of significant biogeochemical and ecological consequence but have received little attention in the context of recent extreme ocean conditions in the Northeast Pacific ocean. Using measurements from multiple satellite sensors we quantify SST, Chla and frontal frequencies off the California and Baja California coasts to place 2014–2016 observations in the context of approximately two decades of variability including previous extremes observed during the 1997–1998 El Niño.

## 2. Methods

### 2.1. Chlorophyll and sea surface temperature data

Satellite data for front detection were downloaded as level-2 datasets of SST (°C) and Chla (*chlor_a*, mg m$^{-3}$) with approximately 1-km spatial resolution from the NASA Ocean Color Web (https://oceancolor.gsfc.nasa.gov). Ocean color data had been produced by NASA with the standard algorithms (O'Reilly et al., 1998; Hu et al., 2012) using the latest calibrations. For Chla those were, respectively, processing versions 2014.0 for OCTS (1996–1997), 2014.0 for SeaWiFS (1997–2010), 2014.0.1 for MODIS-Aqua (MODISA, 2002–2017) and 2014.01.2 for VIIRS-NPP (2012–2017). For SST the processing versions were, respectively, 2014.01.1 for both MODIS-Terra (2000–2017) and MODIS-Aqua (2002–2017) and 2016.0 for VIIRS-NPP (2012–2017). Both Chla and SST level-2 datasets were mapped to an Albers conic equal area map with 1-km$^2$ pixel size (http://wimsoft.com/CAL/files/). Chla datasets were converted to log10 scaling from 0.01 to 64 mg m$^{-3}$ and SST datasets to linear scaling with a step of 0.15 °C.

The abovementioned datasets were used for front detection as they are sufficiently accurate and have the highest available spatial resolution needed for front detection. For creating longer time series of both SST and Chla we used different datasets as the SST dataset mentioned above started only in 2000 and the standard Chla datasets were not produced with the optimal algorithm for our region. SST time series and the respective anomalies were created from the version 2.0 daily datasets of optimally interpolated global blended AVHRR temperatures (Reynolds et al., 2007) (https://podaac.jpl.nasa.gov/dataset/AVHRR_OI-NCEI-L4-GLOB-v2.0). Chla time series and the respective anomalies were created using the regionally optimized algorithms (Kahru et al., 2012b, 2015) applied to daily spectral remote sensing reflectance data of multiple satellite sensors at 4 km resolution (http://www.wimsoft.com/CC4km.htm). The various satellite sensors used for different target variables are listed in Table 1.

SST anomalies were expressed as differences from the respective

**Table 1**
Satellite sensors used in the analysis.

| Target variable | Sensors used | Time range |
| --- | --- | --- |
| Front frequency of Chla | OCTS, SeaWiFS, MODIS-Aqua, VIIRS-NPP | 1996–2017 |
| Front frequency of SST | MODIS-Terra, MODIS-Aqua, VIIRS-NPP | 2000–2017 |
| Time series of Chla | OCTS, SeaWiFS, MERIS, MODIS-Aqua, VIIRS-NPP | 1996–2017 |
| Time series of SST | AVHRR-OI | 1982–2017 |

monthly climatological means ($SST_A = SST - SST_C$). As Chla values are log-normally distributed, Chla anomalies were calculated as ratios to the respective monthly climatology means ($Chla_A = Chla/Chla_C$). The Chla ratio anomaly was then expressed as a percentage with $Chla_{RA} = 100 * (Chla_A - 1)$.

### 2.2. Front detection

The detection of fronts using satellite data is highly sensitive to the characteristics of the data, such as spatial resolution, signal to noise ratio, swath width and contamination by clouds, sun glint, etc. As availability of visible and infrared satellite data is limited by the presence of clouds, individual datasets are often composited into multi-day or monthly images, which are then used for front detection. However, composited datasets often contain artificial discontinuities that may resemble fronts and should therefore not be used for mesoscale front detection. In this study we detected fronts using only uncomposited satellite data from individual sensors and then merged the detected fronts to compute frontal frequencies over certain time periods.

For front detection we used the histogram method (Cayula and Cornillon, 1992; Diehl et al., 2002; Kahru et al., 2012a), which searches for bimodality of histograms calculated for overlapping windows of an image. In order to reduce pixel-to-pixel variance the daily mapped datasets of individual sensors were first averaged in 2 × 2 pixel windows (i.e., the image resolution was reduced by a factor of 2) and then front detection was applied using windows of 32 × 32 pixels. As the method assumes at least three contiguous pixels to be classified as a front, the minimum size of detectable fronts is about 6 km. For each daily image front pixels as well as valid data pixels were detected. By accumulating the counts of front detections (*Nfront*) and valid detections (*Nvalid*) for each pixel over a given time interval, we calculated frontal frequency (*Ff*) as the ratio of the number of detected fronts per pixel to the number of valid views of the pixel (*Nfront/Nvalid*, Kahru et al., 2012b). In this work we used a month as the time interval but we also experimented with a 15-day period, which produced similar results. By using a monthly period of compositing, most pixels have at least some coverage during the period. *Ff* for Chla (*FfChl*) was calculated individually for each of the daily datasets of OCTS, SeaWiFS, MODISA and VIIRS. Pixelwise counts of fronts and valid pixels from multiple sensors were added for overlapping periods and *Ff* was again calculated as a ratio of the two. A similar process was applied to calculate frontal frequency of SST (*FfSst*) by using daily datasets of the MODIS sensor on the Terra (MODIST) and Aqua (MODISA) platforms and VIIRS on SNPP. All these datasets are quite similar in their spatial characteristics and the detected frontal frequencies were compatible. However, due to the use of high-resolution MODIS and VIIRS data, our time span for detecting SST fronts was limited to 2000–2017 while chlorophyll fronts were detected for 1997–2017. In Kahru et al. (2012a) we used global 4-km AVHRR data for detecting SST fronts and Chla data were downgraded to the same resolution. As both the absolute values of *Ff* and their spatial patterns are dependent on the spatial resolution of input data, the *Ff* values produced in this work are not directly comparable to those in Kahru et al. (2012a).

It is important to note that the histogram front detection method used here depends on the detection of contiguous clusters of pixels corresponding to separate peaks in the histogram and does not depend on the strength of the gradient, i.e. the strength of the front. Therefore, maps of frontal frequency presented here do not differentiate between fronts of different strength. Satellite data are often contaminated by erroneous pixel values, e.g. due to undetected or sub-pixel clouds, glint, etc. The histogram method is well suited to deal with erroneous pixels that reduce its ability to detect fronts but do not normally produce fortuitous fronts due to erroneous pixels. The gradient method on the other hand is very sensitive to erroneous pixels. The emphasis of this paper is on the relatively small-scale fronts (6 km and longer) that cannot be detected by passive infrared sensors or satellite altimetry
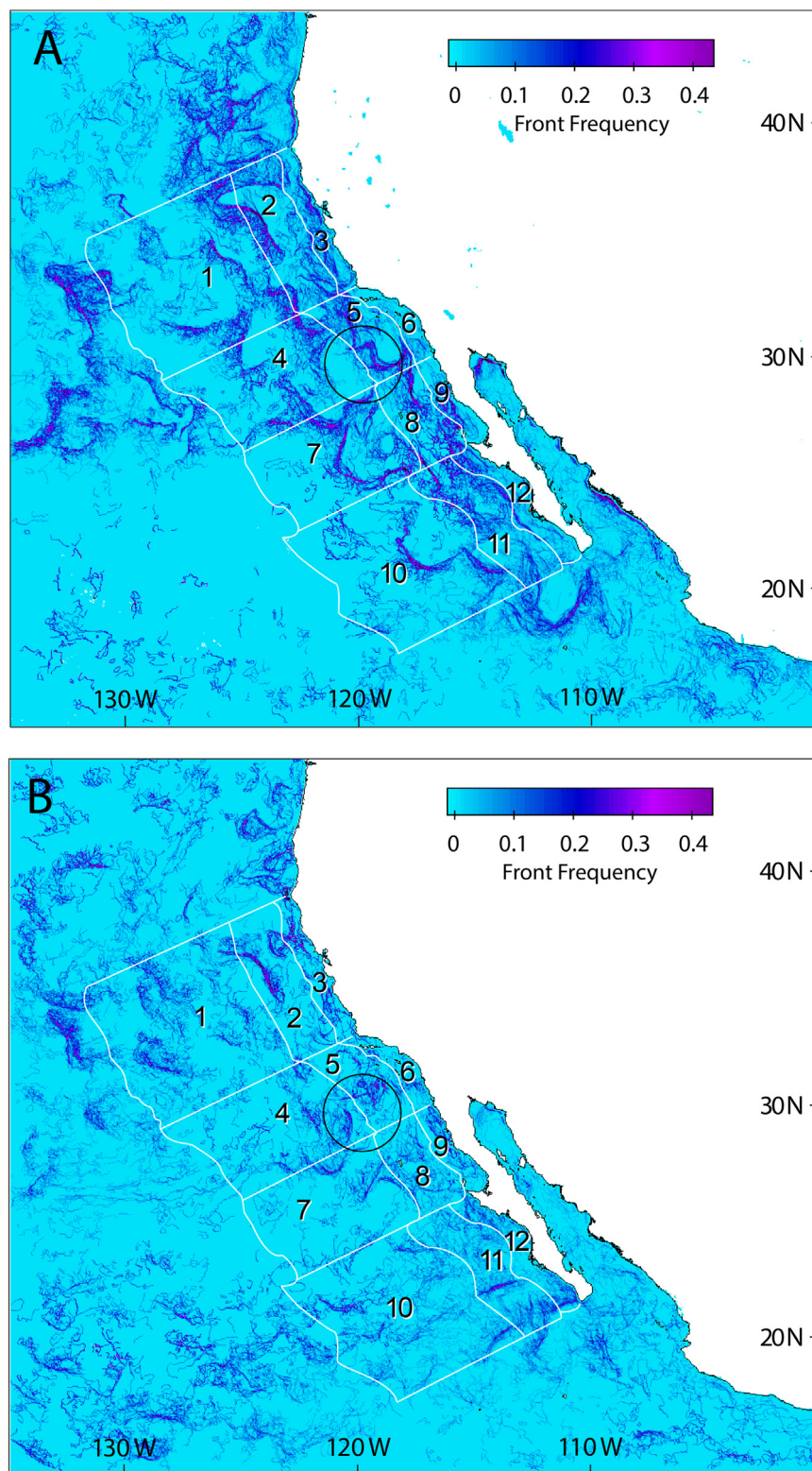
**Fig. 1.** Patterns of front frequency for August 2003. (A) Chla front frequency (*FfChl*); (B) SST front frequency (*FfSst*). Numbers 1–12 are labels of a grid of 4 × 3 sub-areas; the black circle shows the location of the Ensenada front area and has an approximate diameter of 370 km (~200 nautical miles).

(which both have low spatial resolution) but can be detected with ~1 km satellite imagery. On the other hand, large-scale fronts are better detected by satellite data that are not limited by clouds (e.g., microwave or altimetry) or imagery that has been heavily composited to fill gaps due to missing data (e.g., due to clouds).

Annual mean cycles of front frequencies were calculating by averaging all respective monthly composites. Time series of *Ff* for each sub-domain were calculated by averaging the pixel values of *Ff* in the domain and monthly anomalies of *Ff* were calculated by subtracting the mean monthly *Ff* from the monthly *Ff* of each individual month.

Time series of frontal frequencies in different domains were calculated by averaging *Ff* for each pixel in the domain of the monthly *Ff*
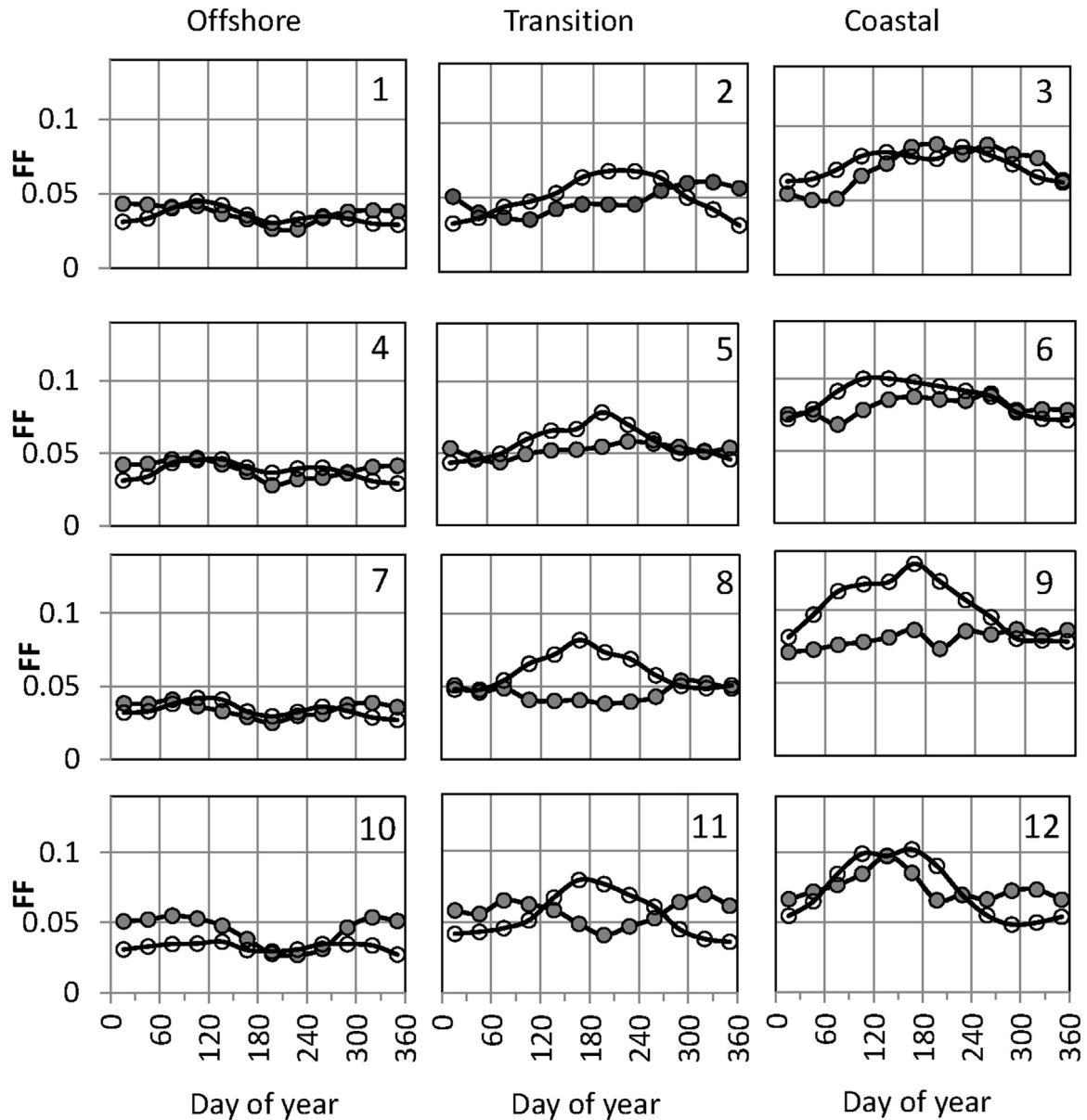
**Fig. 2.** Mean annual cycles of monthly Chla front frequency (*FfChl*, open circles) and SST front frequency (*FfSst*, filled circles) in the California Current areas corresponding to the grid of 3 × 4 sub-domains in Fig. 1.

composite. As a set of spatial domains, we chose 3 × 4 sub-areas in coastal (0–100 km from coast), transition (100–300 km from coast) and offshore (300–1000 km from coast) regions off central and southern California, and northern and southern Baja California (Fig. 1). Additionally, time series were evaluated in a circular area with a diameter of ~370 km (~200 nautical miles), the so-called Ensenada front area (Fig. 1), where multiple previous studies have been conducted (Kahru at al, 2012a, Landry et al., 2012, Ohman et al., 2012). The Ensenada front area was chosen as it is an area of persistent strong fronts and seems to be sensitive to large scale processes in the California Current.

## 3. Results and discussion

### 3.1. Spatial and temporal distributions of fronts

Fig. 1 shows examples of the distribution of fronts in August 2003. In these images, the mean frontal frequency over all ocean area was 2.9% for *FfChl* and 1.8% for *FfSst* with the ratio of standard deviation/ mean being 2.0 for *FfChl* and 2.6 for *FfSst*. The distributions of frontal

frequency values are highly skewed toward low values. A few very high values (close to 1) are based on a few valid pixels and are therefore unreliable. Fronts are typically concentrated in certain areas due to coastal topography and regional hydrography including upwelling, upwelling filaments and currents. For example, in sub-area 9 the mean of *FfChl* was 7.3%, i.e. 2.4 times higher than the mean for the whole image. Some fronts are relatively persistent, such as the Ensenada front and A-Front region (Landry et al., 2012). Patterns of nearby, nearly parallel frontal lines show the spatial advection or transformation of fronts during the observation period of 1 month. While almost all strong fronts have a signature in both SST and Chla, Chla fronts and SST fronts do not necessarily coincide (e.g., Fig. 1), and regionally averaged monthly frontal frequencies for SST and Chla are generally weakly correlated. In fact, of the sub-areas explored in this study, only sub-area 4 off shore of Southern California had a significant correlation between monthly *FfChl* and *FfSst* ($r^2 = 0.25$, $p < 0.05$). This analysis appears to contrast with the glider-based study of Powell and Ohman (2015a), which showed co-occurrence of monthly averaged incidence of SST and Chla fronts, and especially for stronger features. However, the temporal
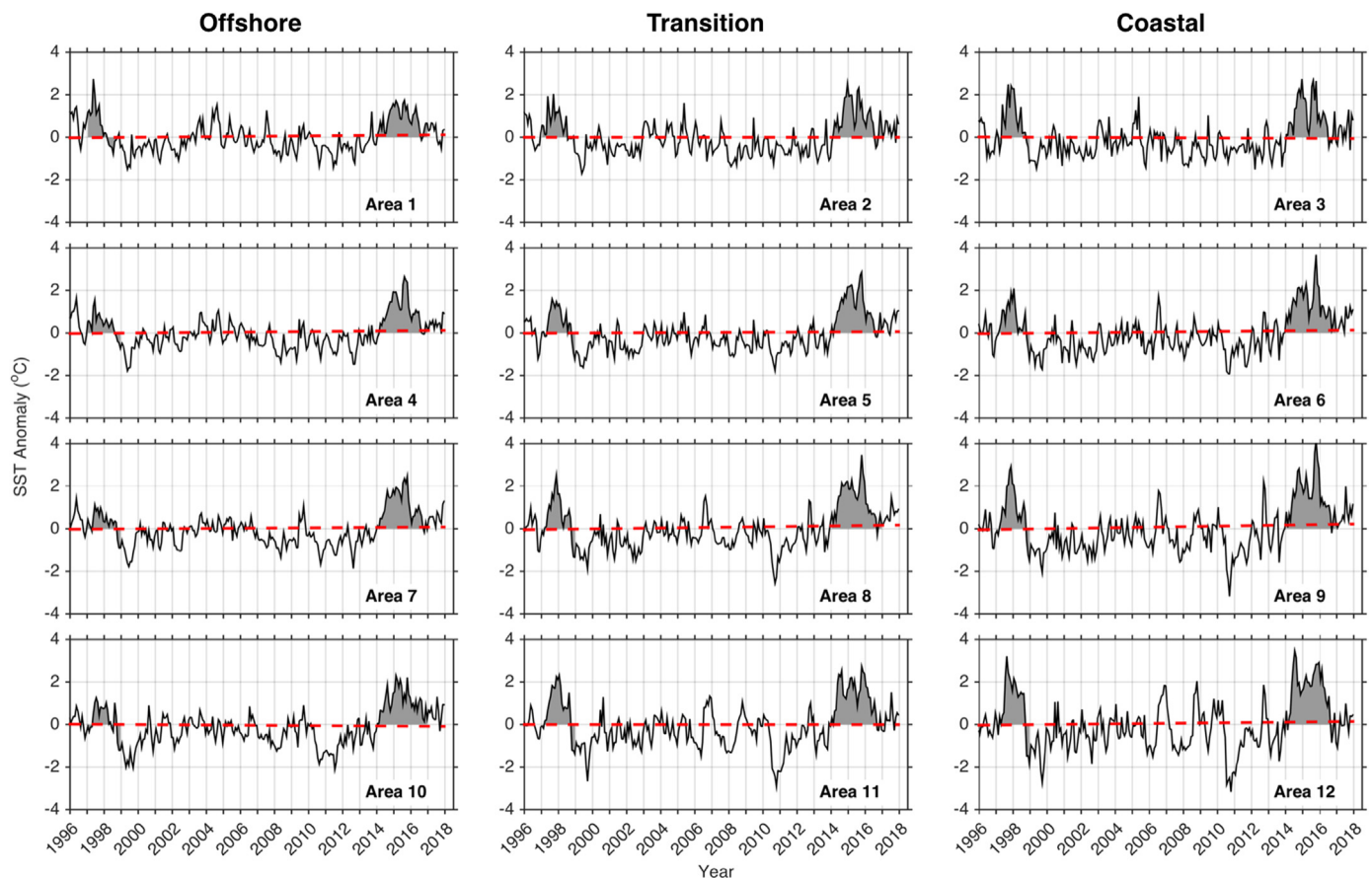
**Fig. 3.** Time series of monthly anomalies of SST (°C) in the grid of 4 × 3 sub-domains in the California Current (see Fig. 1) based on the high-resolution (1 km) datasets. The anomalies of 1997–98 and 2014–16 are shown in gray. Dashed red line is the long-term (1981–2017) linear regression. (For interpretation of the references to color in this figure legend, the reader is referred to the web version of this article.)

correlations reported here do not explicitly evaluate spatial overlap of SST and Chla fronts – rather they quantify whether SST and Chla frontal frequency anomalies averaged within a given region tend to co-vary. Another difference between studies concerns the depths analyzed, which were averaged from 0 to 50 m in Powell and Ohman (2015a), but restricted to surface-expressed features here.

The shape of the mean annual cycle in frontal frequencies is different in different sub-areas (Fig. 2). As expected, there is an obvious increase in frontal frequency from off shore to transition to coastal areas (due to increased mixing of different water masses). In the coastal and transition areas *FfChl* maxima occur in the late spring or summer, while the annual cycle in *FfSst* is weaker and not necessarily in phase with *FfChl*. Summer *FfChl* maxima in coastal and transitional areas coincide with favorable conditions for phytoplankton growth (particularly nutrient supply by seasonal upwelling), suggesting that the seasonal *FfChl* cycle reflects the process of spatially patchy growth of phytoplankton while there is no significant increase in the frequency of SST fronts. This difference between the increased *FfChl* and relatively low *FfSst* is particularly evident in sub-areas 8 and 9 off northern Baja California. Low spatial contrast in surface SST in so-called "hot spots" (Kahru et al., 1993) may be due to a thermal microlayer that forms at the surface in low wind and high solar flux conditions and prevents dectection of the underlying colder water, while ocean color sensors retrieve information from the much deeper layer. In contrast to coastal and transition areas, offshore areas (sub-areas 1, 4, 7, 10) exhibit summer minima for both *FfChl* and *FfSst*, and stronger correlations between the two.

In order to better reveal interannual changes in Chla and SST and in their frontal frequencies, the mean annual cycle was removed from the respective monthly values to obtain time series of monthly anomalies

(Figs. 3–6).

### 3.2. 2014–2016 anomalies in the context of recent decades

The 2014–16 SST anomalies were comparable to the extreme anomalies during the 1997–98 El Niño and in most sub-areas were even more pronounced and persistent (Fig. 3). Positive SST anomalies in the CCS generally correspond to negative Chla anomalies, except in offshore and transition areas off Baja California (Fig. 4, sub-areas 7, 8, 10, 11) where the high SST during the 1997–98 El Niño was associated with increased Chla. Kahru and Mitchell (2000) showed that both of the strong El Niños of 1982–83 and 1997–98 caused reduction in eutrophic chlorophyll areas (i.e. areas with Chla > 1 mg m$^{-3}$) everywhere in CCS (presumably due to reduced upwelling), but an increase in mesotrophic chlorophyll areas (with Chla between 0.2 and 1 mg m$^{-3}$) off Baja California. They hypothesized that the latter was caused by blooms of nitrogen-fixing cyanobacteria in warm stratified waters. Although there were no strong positive anomalies off Baja California in 2014–16, the negative Chla anomalies were weakest in area 11 (offshore southern Baja) while strong negative anomalies dominated in most sub-areas (Fig. 4). Time series of Chla anomalies show weak (but not significant, $p > 0.05$) decreasing trends in almost all sub-areas except in the central California upwelling area (sub-area 3) where there is a weak increasing trend and in southern California (sub-area 6) with no trend evident. Time series of *FfChl* and *FfSst* (Figs. 5 and 6) anomalies show intense month to month variability, with only the coastal region off southern Baja (area 12) exhibiting significant ($p < 0.05$) declining trends in both *FfChl* and *FfSst*. The decreasing trends in both Chla and *FfChl* anomalies off southern Baja California may be related to changing
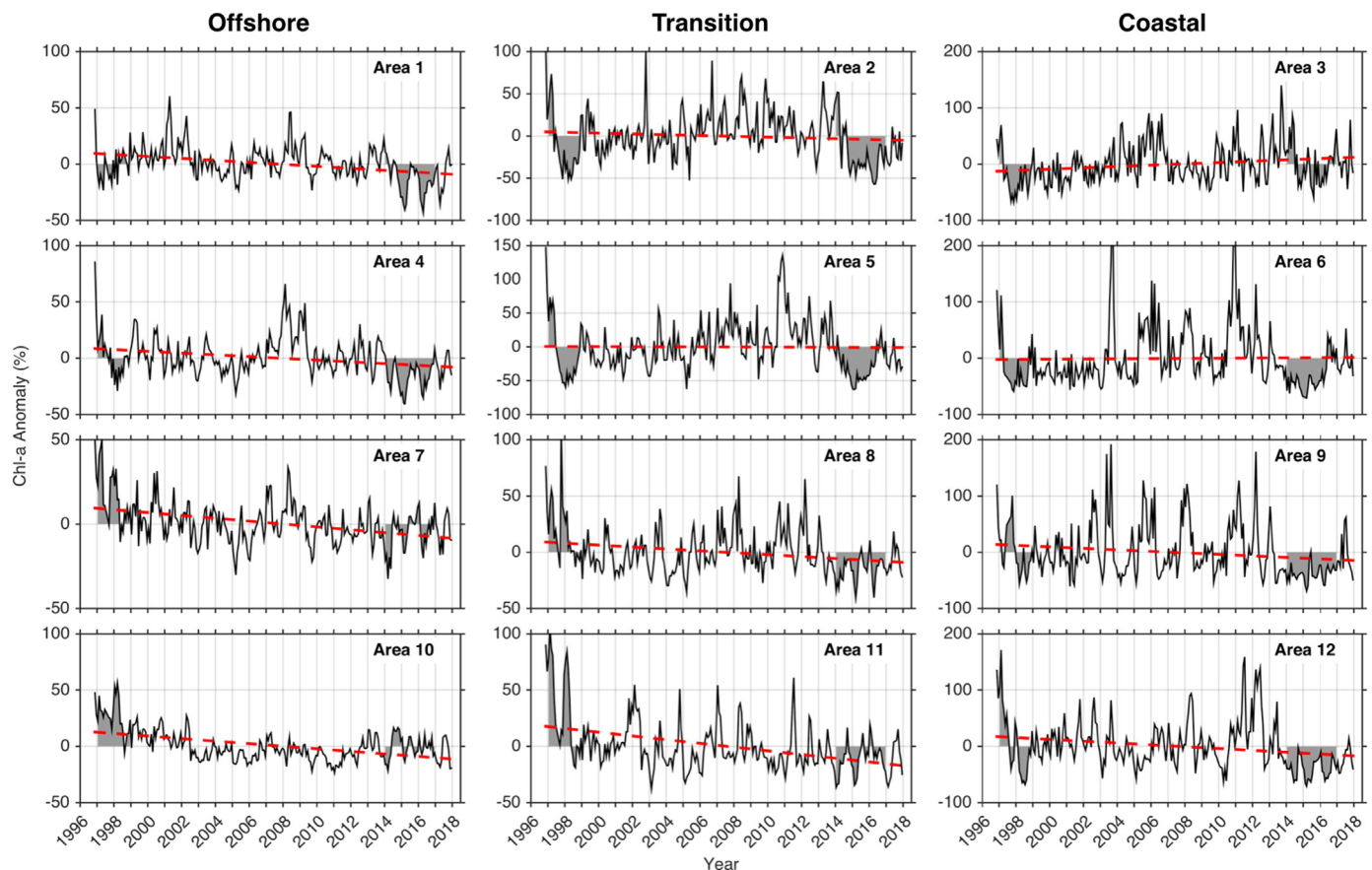
**Fig. 4.** Time series of monthly Chla anomalies (%) in the grid of 4 × 3 sub-domains in the California Current (see Fig. 1). The mostly negative anomalies of 1997–98 and 2014–16 are shown in gray. Dashed red line is the long-term (1996–2017) linear regression. (For interpretation of the references to color in this figure legend, the reader is referred to the web version of this article.)

tropical trade winds and increasing oxygen minimum zones since the 1990s (Deutsch et al., 2014), but these relationships need further study.

Positive SST and negative Chla anomalies from 2014 to 2016 were generally accompanied by negative (though noisy) SST and Chla frontal frequency anomalies. Negative frontal frequency anomalies were particularly evident in the coastal regions, likely related to anomalous weak northerly winds and resultant weakening of filaments, jets, and eddy activity. Spring/early summer 2015 saw a brief reduction in SST anomalies driven by a strong upwelling season that immediately preceded the remote oceanic forcing associated with the 2015–2016 El Niño. Similarly, Chla and frontal frequency anomalies became less negative and in some cases positive in spring/summer 2015, as upwelling favorable winds stimulated phytoplankton growth and more energetic mesoscale circulation.

Some characteristic features of relationships between Chla and frontal frequencies emerge from pixelwise correlations between different variables (Fig. 7). Chla and SST frontal frequencies are generally positively correlated (Fig. 7A) except in the Gulf of California where strong thermal stratification in the summer suppresses SST patterns visible in infrared satellite imagery but not the Chla patterns originating from a deeper layer (e.g. Kahru et al., 2004). *FfChl* and Chla anomalies in the coastal and transition zones of central California (e.g., Areas 2, 3) showed weakly negative correlation between each other (Fig. 7B). This result suggests that in these regions, relationships between Chla and *FfChl* anomalies are driven by different dynamics than those driving their seasonal cycles, which are positively correlated. Opposite *FfChl* and Chla anomaly signatures are evident particularly in the highly anomalous periods on record (1997–98 and 2014–16), when negative Chla anomalies in Areas 2 and 3 were accompanied by positive *FfChl* anomalies. The mostly positive correlations between *FfSst* and Chla

indicate the generally positive influence of thermal fronts on phytoplankton growth in the California Current (Fig. 7C) while the negative correlations between *FfSst* and Chla in the narrow nearshore band in the California Current upwelling area can be explained by the low Chla in recently upwelled waters. Zooplankton distribution and population dynamics are affected by the occurrence of SST and Chla fronts, and zooplankton grazing can affect Chla. However, while theoretically plausible we have no data indicating that zooplankton grazing creates Chla fronts.

For more detailed analysis we have chosen the Ensenada Front region (see Fig. 1) where our earlier analysis (Kahru et al., 2012a), conducted in 2011 and using different satellite datasets, showed significant increasing trends of frontal frequencies. Our current analysis using an extended time series confirms (Fig. 8) that, indeed, both *FfChl* and *FfSst* had increasing trends until about 2011, but decreased after that time and reached local minima during the 2014–2015 warm anomalies. Since 2014–2015 both *FfChl* and *FfSst* have started to increase again (Fig. 8), in conjunction with increasing Chla concentration and decreasing SST (Fig. 9). Interannual variations in the time series of *FfChl* roughly follow the respective annual Chla anomaly time series, while interannual variations in *FfSst* are close to an inverse of the respective annual SST anomaly time series (cf. Figs. 8 and 9). *FfChl* showed sustained low values in 2014, an increase in mid-2015, then a decrease again during the 2015–16 El Niño (Fig. 8). Comparably low values in *FfChl* had not been seen in a sustained manner since El Niño of 1997–98. *FfSst* showed a similar decline in 2014 and transient recovery in spring 2015, then secondary decline in 2015–16.

The short period of transition from the warm anomaly in 2014 to the 2015–16 El Niño in early 2015 (black arrow in Fig. 9B) was also detected in the SST of coastal sub-areas (Fig. 3). The respective Chla
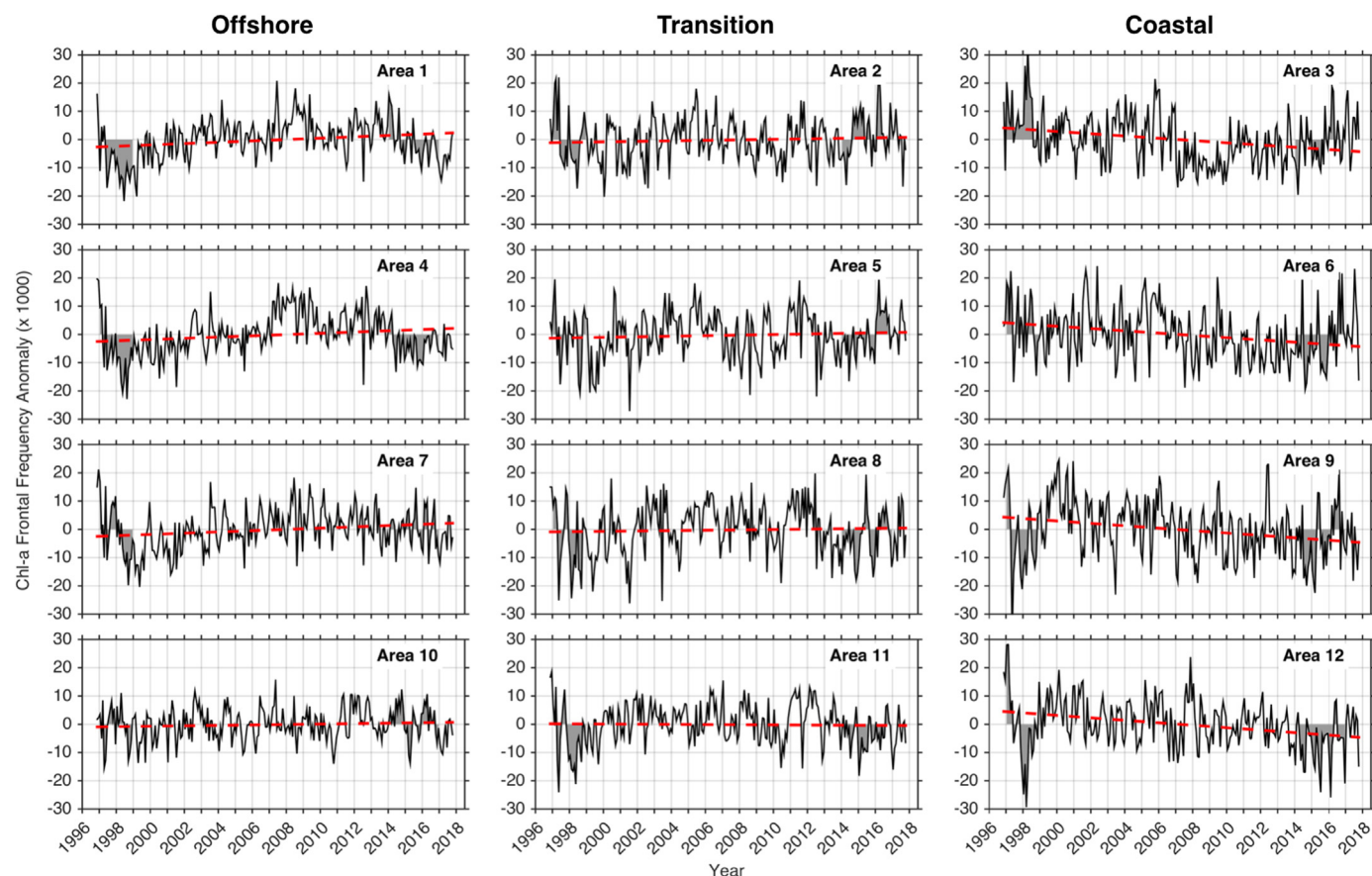
**Fig. 5.** Time series of monthly *FfChl* anomalies (x1000) in the grid of 4 × 3 sub-domains in the California Current (see Fig. 1). The anomalies of 1997–98 and 2014–16 are shown in gray. Dashed red line is the long-term (1996–2017) linear regression. (For interpretation of the references to color in this figure legend, the reader is referred to the web version of this article.)

anomaly in the Ensenada front area (Fig. 9A) did not show the bimodal structure, but there was an uptick in *FfChl* in 2015 (Fig. 8A). The bimodal structure of Chla anomalies in some sub-areas (e.g., areas 1 and 3; Fig. 4), corresponding to the transition phase in early 2015, can also be seen as a few months of positive values amidst the generally depressed values of both *FfChl* and *FfSst* (Fig. 8). While the existence of a short period of interruption between the 2014–15 and 2015–16 anomaly periods can be used to clarify the different forcing mechanisms for the respective events, the duration of transition can be difficult to discern from satellite data with incomplete daily coverage.

In many sub-areas of the California Current System, including the Ensenada front region, the 2014–16 anomalies in both Chla and SST exceeded those of the 1997–98 El Niño and were unprecedented during the whole period of availability of satellite observations, i.e., 1981–2017 for SST and 1996–2017 for Chla.

While the time series of Chla anomalies were generally positively correlated with *FfChl* and *FfSst* on monthly and annual timescales (Fig. 10), the correlations were significant ($p < 0.05$) only for annual averages. The 2014–15 warm anomaly period corresponded to almost uniformly low Chla (around − 50% anomaly) but a rather wide range of *FfChl* and *FfSst*, resulting in no correlation for this period. The generally positive relationship between frontal frequency and Chla can be causal in several ways. First, as most fronts involve tilted isopycnals, they can inject (lift) nutrients into the euphotic zone and/or provide vertical stability needed for phytoplankton growth, leading to higher chlorophyll concentrations. On the other hand, high phytoplankton growth rates and resulting high Chla driven by processes other than fronts (e.g., coastal upwelling) can naturally lead to increased Chla patchiness and consequently to Chla fronts.

### 3.3. Potential connections to the ocean carbon pump

Fronts are intimately involved in many ocean processes including the ocean's ability to serve as a $CO_2$ sink (Stukel et al., 2017). It appears that the annual cycle in the balance of marine autotrophy and heterotrophy and particularly the potential export efficiency (out of the euphotic zone) at the San Pedro station (near the center of sub-area 6 in Fig. 1) in the coastal zone of Southern California (Haskell et al., 2017) is well correlated with the onset of the annual cycle in the frequency of Chla fronts in the area (Fig. 11). The sharp increase in the ratio of net:gross oxygen production (NOP/GOP), which is an estimate of potential export efficiency, coincides with the rise in *FfChl* in the area. It is likely that both increase sharply with the spring onset of upwelling while the summer increase in *FfChl* does not seem to have an effect on NOP/GOP. While any suggestion of causality between these variables is speculative, the frontal frequency could perhaps be useful as a proxy to estimate biological export of carbon out of the euphotic zone. Continental margins, especially coastal upwelling regions, account for a disproportionately large amount of carbon export but current global models of carbon export using simple relationships with primary production and SST are inaccurate in the upwelling waters of CCS (Kelly et al., in this issue).

### 4. Conclusions

The effects of the North-East Pacific warm anomalies of 2014–2016 resulted in high SST and low Chla anomalies in the California Current System that were unprecedented in the whole period of availability of satellite observations (1982–2017 for SST and 1996–2017 for Chla). At the same time, the frequency of surface SST and Chla fronts were

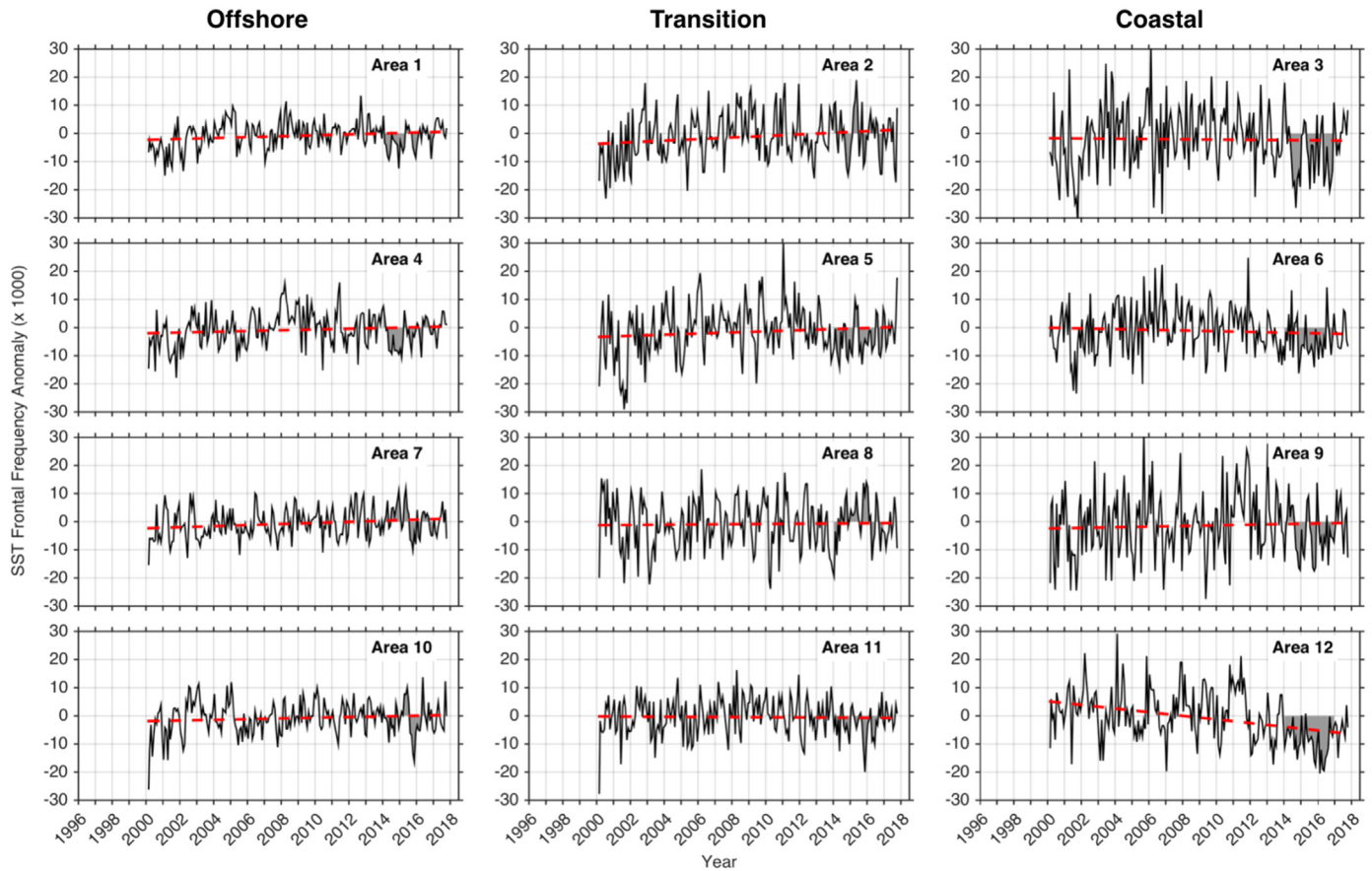**Fig. 6.** Time series of monthly *FfSst* anomalies (x1000) in the grid of 4 × 3 sub-domains in the California Current (see Fig. 1). The anomalies of 2014–16 are shown in gray. Dashed red line is the long-term (2000–2017) linear regression. (For interpretation of the references to color in this figure legend, the reader is referred to the web version of this article.)
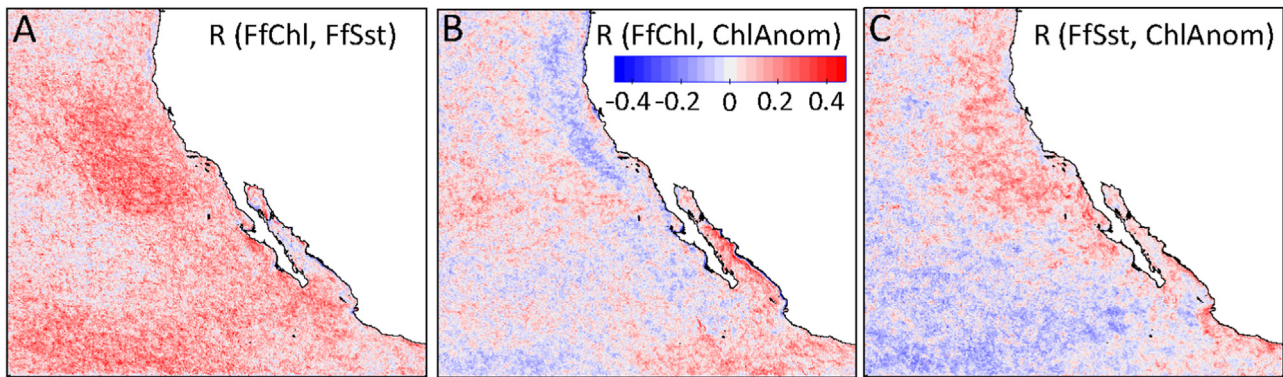


**Fig. 7.** Spatial patterns of the pixelwise correlation coefficient between monthly time series of (A) *FfChl* and *FfSst* (2000–2017), (B) *FfChl* and Chla anomalies (1996–2017) and (C) *FfSst* and Chla anomalies (2000–2017).

significantly reduced, though the minima were not lower than those during the 1997–98 El Niño. The annual cycle of the frequency of surface Chla fronts in the coastal zone of Southern California is closely related to an estimate of potential export efficiency (NOP/GOP), and both are likely associated with the spring onset of upwelling. It remains to be seen whether recent declines in *FfSst* and *FfChl* are merely interruptions in the long terms increasing trends reported by Kahru et al. (2012a) or whether they represent the beginning of a longer-lived declining trend in frontal frequency. Previous studies have demonstrated that apparent trends of physical and biogeochemical variables in the CCS of even multi-decadal duration can result from natural variability rather than secular change (e.g., Jacox et al., 2015; Henson et al.,

2016), and the same seems likely to be true for frontal frequency. Given the demonstrated importance of oceanic fronts to the physical, biogeochemical, and ecological functioning of the CCS, long observational records of frontal activity like those presented here will aid our understanding of ecosystem dynamics and their relation to climate variability and change over a range of spatiotemporal scales.
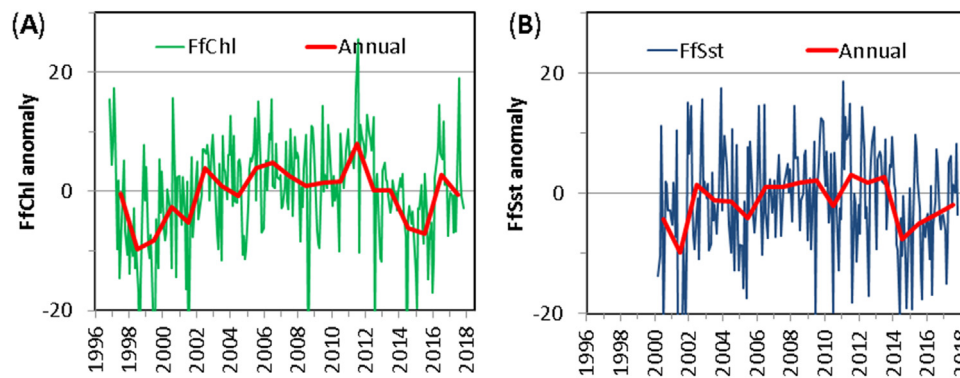
### Acknowledgements

**Fig. 8.** Time series of monthly anomalies (x1000) of *FfChl* (A) and *FfSst* (B) as well as their respective annual averages (red lines) in the Ensenada front area. (For interpretation of the references to color in this figure legend, the reader is referred to the web version of this article.)
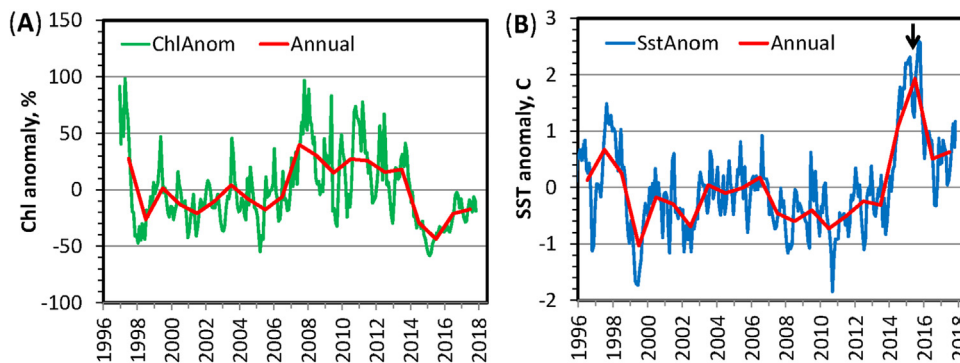


**Fig. 9.** Time series of monthly anomalies of (A) Chla (%) and (B) SST (°C) as well as their respective annual averages (red lines) in the Ensenada front area. The black arrow in B shows the short drop in high anomalies in early 2015. (For interpretation of the references to color in this figure legend, the reader is referred to the web version of this article.)
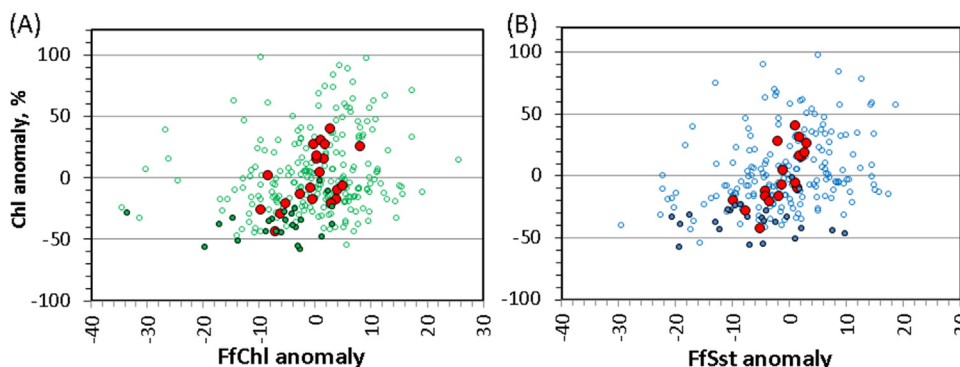


**Fig. 10.** Relationships of Chla anomalies (vertical axis) with (A) *FfChl* and (B) *FfSst* anomalies (x1000) for monthly means (open circles), monthly means for 2014–2015 (filled circles) and annual means (large, red filled circles). (For interpretation of the references to color in this figure legend, the reader is referred to the web version of this article.)
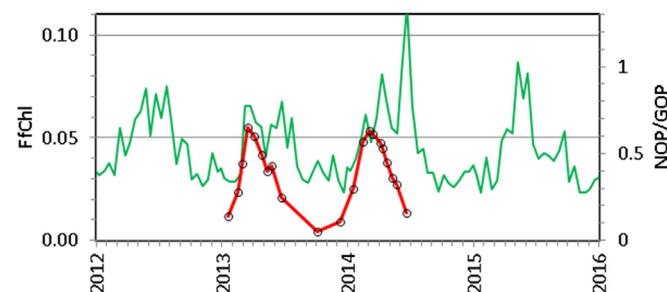


**Fig. 11.** Time series of the frequency of Chla fronts (green line, left axis) calculated for 15-day intervals in the center of sub-area 6 and the ratio of net oxygen production to gross oxygen production (open circles, red line right axis; data from Haskell et al., 2017) at San Pedro station in coastal zone of Southern California (sub-area 6). (For interpretation of the references to color in this figure legend, the reader is referred to the web version of this article.)

Biogeochemistry NNX14 A.M.15G.

### Data availability

Archive of the monthly frontal frequencies of Chla and SST (1996–2017 for *FfChl*, 2000–2017 for *FfSst*) in the California Current System are available at: https://drive.google.com/open?id=1ohJeinQlUSokG-Pqit1hJ8BIbvRiWSV1. Both 2-km and 4-km spatial resolutions are provided in PNG and HDF4 formats.

### References

Belkin, I.M., 2009. Observational studies of oceanic fronts. J. Mar. Syst. 78, 317–318.

Bernstein, R.L., Breaker, L., Whritner, R., 1977. California Current eddy formation: ship, air and satellite results. Science 195, 353–359.

Bond, N.A., Cronin, M.F., Freeland, H., Mantua, N., 2015. Causes and impacts of the 2014 warm anomaly in the NE Pacific. Geophys. Res. Lett. 42, 3414–3420. http://dx.doi.org/10.1002/2015GL063306.

Castelao, R.M., Mavor, T.P., Barth, J.A., et al., 2006. Sea surface temperature fronts in the California Current System from geostationary satellite observations. J. Geophys. Res. 111. http://dx.doi.org/10.1029/2006JC003541.

Cavole, L.M., Demko, A.M., Diner, R.E., Giddings, A., Koester, I., Pagniello, C.M., Paulsen, M.L., Ramirez-Valdez, A., Schwenck, S.M., Yen, N.K., Zill, M.E., 2016. Biological impacts of the 2013–2015 warm-water anomaly in the Northeast Pacific: winners, losers, and the future. Oceanography 29 (2), 273–285.

Cayula, J.-F., Cornillon, P., 1992. Edge detection algorithm for SST images. J. Atmos. Ocean. Technol. 9, 67–80.

Di Lorenzo, E., Mantua, N., 2016. Multi-year persistence of the 2014/15 North Pacific marine heatwave. Nat. Clim. Change 6 (11), 1042–1047.

Deutsch, C., Berelson, W., Thunell, R., Weber, T., Tems, C., McManus, J., Crusius, J., Ito, T., Baumgartner, T., Ferreira, V., Mey, J., van Geen, A., 2014. Centennial changes in North Pacific anoxia linked to tropical trade winds. Science 345 (6197), 665–668. http://dx.doi.org/10.1126/science.1252332.

Diehl, S.F., Budd, J.W., Ullman, D., 2002. Geographic window sizes applied to remote sensing sea surface temperature front detection. J. Atmos. Ocean. Technol. 19 (1115-1113).

Flament, P., Armi, L., Washburn, L., 1985. The evolving structure of an upwelling filament. J. Geophys. Res. 90, 11765–11778. http://dx.doi.org/10.1029/JC090iC06p11765.

Frischknecht, M., Münnich, M., Gruber, N., 2017. Local atmospheric forcing driving an unexpected California Current System response during the 2015–2016 El Niño. Geophys. Res. Lett. 44 (1), 304–311.

Gentemann, C.L., Fewings, M.R., García-Reyes, M., 2017. Satellite sea surface temperatures along the West Coast of the United States during the 2014–2016 northeast Pacific marine heat wave. Geophys. Res. Lett. 44 (1), 312–319.

Gómez-Ocampo, E., Gaxiola-Castro, G., Durazo, R., Beier, E., 2017. Effects of the 2013–2016 warm anomalies on the California Current phytoplankton. Deep Sea Res. Part II: Top. Stud. Oceanogr.

Haskell II, W.Z., Prokopenko, M.G., Hammond, D.E., Stanley, R.H., Sandwith, R.Z.O., 2017. Annual cyclicity in export efficiency in the inner Southern California Bight. Glob. Biogeochem. Cycles 31, 1–20. http://dx.doi.org/10.1002/2016GB005561.

Henson, S.A., Beaulieu, C., Lampitt, R., 2016. Observing climate change trends in ocean biogeochemistry: when and where. Glob. Change Biol. 22 (4), 1561–1571.

Hu, C., Lee, Z., Franz, B., 2012. Chlorophyll a algorithms for oligotrophic oceans: a novel approach based on three-band reflectance difference. J. Geophys. Res. 117, C01011. http://dx.doi.org/10.1029/2011JC007395.

Jacox, M.G., Bograd, S.J., Hazen, E.L., Fiechter, J., 2015. Sensitivity of the California Current nutrient supply to wind, heat, and remote ocean forcing. Geophys. Res. Lett. 42, 5950–5957. http://dx.doi.org/10.1002/2015GL065147.

Jacox, M.G., Hazen, E.L., Zaba, K.D., Rudnick, D.L., Edwards, C.A., Moore, A.M., Bograd, S.J., 2016. Impacts of the 2015–2016 El Niño on the California Current System: early assessment and comparison to past events. Geophys. Res. Lett. 43, 7072–7080. http://dx.doi.org/10.1002/2016GL069716.

Jacox, M.G., Alexander, M.A., Mantua, N.J., Scott, J.D., Hervieux, G., Webb, R.S., Werner, F.E., 2017. Forcing of multiyear extreme ocean temperatures that impacted California Current living marine resources in 2016 [in "Explaining extreme events of 2016 from a climate perspective"]. Bull. Am. Meteorol. Soc. 98, S27–S33. http://dx.doi.org/10.1175/BAMS-D-17-0119.1.

Kahru, M., Leppänen, J.-M., Rud, O., 1993. Cyanobacterial blooms cause heating of the sea surface. Mar. Ecol. Prog. Ser. 101, 1–7.

Kahru, M., Mitchell, B.G., 2000. Influence of the 1997-98 El Niño on the surface chlorophyll in the California Current. Geophys. Res. Lett. 27 (18), 2937–2940.

Kahru, M., Marinone, S.G., Lluch-Cota, S.E., Pares-Sierra, A., Mitchell, B.G., 2004. Ocean color variability in the Gulf of California: scales from tides to ENSO. Deep-Sea Res. II 51, 139–146.

Kahru, M., Di Lorenzo, E., Manzano-Sarabia, M., Mitchell, B.G., 2012a. Spatial and temporal statistics of sea surface temperature and chlorophyll fronts in the California Current. J. Plankton Res. 34 (9), 749–760. http://dx.doi.org/10.1093/plankt/fbs010.

Kahru, M., Kudela, R.M., Manzano-Sarabia, M., Mitchell, B.G., 2012b. Trends in the surface chlorophyll of the California Current: merging data from multiple ocean color

satellites. Deep Sea Res. II 77–80, 89–98. http://dx.doi.org/10.1016/j.dsr2.2012.04.007.

Kahru, M., Kudela, R.M., Anderson, C.R., Mitchell, B.G., 2015. Optimized merger of ocean chlorophyll algorithms of MODIS-Aqua and VIIRS. IEEE Geosci. Remote Sens. Lett. 12, 11. http://dx.doi.org/10.1109/LGRS.2015.2470250.

Kelly, T.B., Goericke, R., Kahru, M., Song, H., Stukel, M.R., 2018. Spatial and interannual variability in export efficiency and the biological pump in an eastern boundary current upwelling system with substantial lateral advection. Submitted to Deep Sea Res. Part II Top. Stud. Oceanogr. XXX, X–X (in this issue).

Landry, M.R., Ohman, M.D., Goericke, R., Stukel, M.R., Barbeau, K., Dundy, R., Kahru, M., 2012. Pelagic community responses to a deep-water front in the California Current Ecosystem: overview of the A-Front Study. J. Plankton Res. 34 (9), 739–748.

McCabe, R.M., Hickey, B.M., Kudela, R.M., Lefebvre, K.A., Adams, N.G., Bill, B.D., Gulland, F., Thomson, R.E., Cochlan, W.P., Trainer, V.L., 2016. An unprecedented coastwide toxic algal bloom linked to anomalous ocean conditions. Geophys. Res. Lett. 43 (19).

McClatchie, S., Goericke, R., Leising, A., et al., 2016. State of the California Current 2015-16: Comparisons with the 1997-98 El Niño, CalCOFI Reports, 57.

Miller, P.I., Christodoulou, S., 2014. Frequent locations of ocean fronts as an indicator of pelagic diversity: application to marine protected areas and renewables. Mar. Policy 45, 318–329. http://dx.doi.org/10.1016/j.marpol.2013.09.009.

Ohman, M.D., Powell, J.R., Picheral, M., Jensen, D.W., 2012. Mesozooplankton and particulate matter responses to a deep-water frontal system in the southern California Current System. J. Plankton Res. 34 (9), 815–827. http://dx.doi.org/10.1093/plankt/fbs028.

Peterson, W.T., Fisher, J.L., Strub, P.T., Du, X., Risien, C., Peterson, J., Shaw, C.T., 2017. The pelagic ecosystem in the Northern California Current off Oregon during the 2014–2016 warm anomalies within the context of the past 20 years. J. Geophys. Res.: Oceans 122 (9), 7267–7290.

Powell, J.R., Ohman, M.D., 2015a. Covariability of zooplankton gradients with glider-detected density fronts in the Southern California Current System. Deep-Sea Res. Part II 112, 79–90. http://dx.doi.org/10.1016/j.dsr2.2014.04.002.

Powell, J.R., Ohman, M.D., 2015b. Changes in zooplankton habitat, behavior, and acoustic scattering characteristics across glider-resolved fronts in the Southern California Current System. Progr. Oceanogr. 134, 77–92. http://dx.doi.org/10.1016/j.pocean.2014.12.011.

O'Reilly, J.E., Maritorena, S., Mitchell, B.G., Siegel, D.A., Carder, K.L., Garver, S.A., Kahru, M., McClain, C.R., 1998. Ocean color chlorophyll algorithms for SeaWiFS. J. Geophys. Res. 103, 24937–24953.

Reynolds, R.W., Smith, T.M., Liu, C., Chelton, D.B., Casey, K.S., Schlax, G., 2007. Daily high-resolution blended analyses for sea surface temperature. J. Clim. 20, 5473–5496. http://dx.doi.org/10.1175/2007JCLI1824.1.

Scales, K.L., Miller, P.I., Hawkes, L.A., Ingram, S.N., Sims, D.W., Votier, S.C., 2014. Review: on the front line: frontal zones as priority at-sea conservation areas for mobile marine vertebrates. J. Appl. Ecol. 51, 1575–1583. http://dx.doi.org/10.1111/1365-2664.12330.

Strub, P.T., Kosro, P.M., Huyer, A., 1991. The nature of the cold filaments in the California Current system. J. Geophys. Res. 96, 14,743–14,768.

Stukel, M.R., Aluwihare, L.I., Barbeau, K.A., Chekalyuk, A.M., Goericke, R., Miller, A.J., Ohman, M.D., Ruacho, A., Song, H., Stephens, B.M., Landry, M.R., 2017. Mesoscale ocean fronts enhance carbon export due to gravitational sinking and subduction. PNAS 114, 1252–1257 (doi: www.pnas.org/cgi/doi/10.1073/pnas.1609435114).

Woodson, C.B., Litvin, S.Y., 2015. Ocean fronts drive marine fishery production and biogeochemical cycling. PNAS 112, 1710–1715(doi: http://www.pnas.org/content/112/6/1710).

Zaba, K.D., Rudnick, D.L., 2016. The 2014-2015 warming anomaly in the Southern California Current System observed by underwater gliders. Geophys. Res. Lett. 43, 1241–1248. http://dx.doi.org/10.1002/2015GL067550.